







Dual Motor Power Sharing Control for Electric Vehicles With Battery Power Management

Utkal Ranjan Muduli , Senior Member, IEEE, Abdul R. Beig , Senior Member, IEEE, Khaled Al Jaafari , Senior Member, IEEE, Khalifa Al Hosani , Senior Member, IEEE, Ameena Saad Al-Sumaiti , Senior Member, IEEE, and Ranjan Kumar Behera , Senior Member, IEEE

Abstract—Induction motor powertrains are emerging as a cost-effective option for high-power electric vehicles (EVs). A differential four-wheel drive (D4WD) EV based on two open-end winding induction motor (OEWM) propulsion is presented in this article. Each OEWM is driven by two two-level voltage source inverters (VSIs) with two isolated battery packs as the source. The proposed drive control algorithm integrates the uniform state-of-charge (SoC) distribution and fault-tolerant operation. A two-stage lookup table (LUT)-based direct torque control (DTC) scheme is proposed to balance the SoC of batteries by selecting the suitable redundant VSI voltage vectors. The proposed LUT-DTC scheme is less sensitive to variations in motor parameters and provides excellent steady-state and transient performance. The results show the superiority of the proposed controller in terms of battery SoC balancing. The performance of the EV drive with the proposed LUT-DTC is validated by both simulation and laboratory experiments for the FTP75 and HFET driving cycles under different operating modes under normal and fault conditions. The dual-motor-driven D4WD with the proposed LUT-DTC is found to achieve 89.2% efficiency.

Index Terms—Direct torque control (DTC), electric vehicle (EV), open-end winding induction motor (OEWM), propulsion systems, state-of-charge (SoC) control.

Manuscript received 29 July 2022; revised 14 November 2022; accepted 23 December 2022. Date of publication 17 January 2023; date of current version 9 June 2023. The work of Ameena Saad Al-Sumaiti was supported by the NEP 3.0 program. This work was supported in part by Khalifa University, Abu Dhabi, United Arab Emirates, under Advanced Power and Energy Center under Grant *RC2-2018/21-06*; in part by Khalifa University, Abu Dhabi, United Arab Emirates, under Grant *KKJRC-2019-Trans2*; in part by the Advanced Technology Research Council ASPIRE Virtual Research Institute (VRI) Program, Abu Dhabi, United Arab Emirates, under Grant *VRI20-07*; and in part by the Science and Engineering Research Board (SERB), Government of India, under Project No. *EEQ/2021/000119*. (Corresponding author: Utkal Ranjan Muduli.)

Utkal Ranjan Muduli, Abdul R. Beig, Khaled Al Jaafari, Khalifa Al Hosani, and Ameena Saad Al-Sumaiti are with the Advanced Power and Energy Center, Department of Electrical Engineering and Computer Science, Khalifa University of Science and Technology, Abu Dhabi 127788, United Arab Emirates (e-mail: utkal.muduli@ku.ac.ae; balanthi.beig@ku.ac.ae; khaled.aljaafari@ku.ac.ae; khalifa.halhosani@ku.ac.ae; ameena.alsumaiti@ku.ac.ae).

Ranjan Kumar Behera is with the Department of Electrical Engineering, Indian Institute of Technology Patna, Patna 801103, India (e-mail: rkb@iitp.ac.in).

Color versions of one or more figures in this article are available at <https://doi.org/10.1109/TIE.2023.3236096>.

Digital Object Identifier 10.1109/TIE.2023.3236096

NOMENCLATURE

δ	Steering angle of the front wheel axle (rad).
R_w	Effective or rolling radius of each wheel (m).
$l \in \{f, r\}$	Subscript f : front, r : rear
ω_{mf}, ω_{mr}	Mechanical rotor speed of the front and rear OEWMs (rad/s).
$\omega_{mf}^*, \omega_{mr}^*$	Reference mechanical speed for front and rear OEWMs (rad/s).
T_{df}^*, T_{dr}^*	Reference driving torque for the front and rear OEWMs (N.m).
T_{bf}, T_{br}	Braking torque applied to the front and rear OEWMs (N.m).
F_{xf}, F_{xr}	The combined longitudinal force acts on the front and rear wheels (N).
T_{mf}^*, T_{mr}^*	Reference electromagnetic torque for the front and rear OEWMs (N.m).
T_{el}	Estimated electromagnetic torque for the front and rear OEWMs (N.m), $l \in \{f, r\}$.
V_{dc}	DC-link voltage of the VSI (V).
V_{BP1}, V_{BP2}	Terminal voltages of battery pack-1 (BP1) and battery pack-2 (BP2) (V).
$v_{sl}, i_{sl}, \psi_{sl}$	Stator voltage, current, and flux-linkage space vector for front and rear OEWMs (V, A, wb).
$V_{L(q)}, V_{M(q)}$	Large- and medium-voltage vectors for sector $q \in \{1 \dots 6\}$ (V).
$O, V_{S(q)}$	Zero- and small-voltage vectors for sector $q \in \{1 \dots 6\}$ (V).
k	Denotes the present sample of the DSP controller with sampling time T_s .

I. INTRODUCTION

IN ORDER to control pollution, many government agencies around the world are taking steps to develop appropriate policies that limit the use of fossil fuels [1], [2]. One of the measures in this direction is replacing traditional fossil fuel engines with battery-powered electric propulsion drives for buses, trucks, cars, aircraft, and ships [3], [4]. At present, small electric vehicles (EVs), such as bicycles, motorcycles, electric scooters, and small electric cars, contribute only 5% of the total of road vehicles. According to statistics, the percentage of on-road EVs will be around 33% by 2030 [5].

Presently, permanent-magnet synchronous motors (PMSMs) are used as an electric propulsion motor in low-powered EVs [1].

Rare-earth magnetic materials (AlNiCO, samarium-cobalt, and neodymium) are used in PMSMs and are limited and expensive, necessitating the development of suitable alternative drive motors for EVs. Among the other types of motors, the conventional induction motor (IM) is the best solution in this regard in terms of cost, efficiency, control, and robustness [6]. Therefore, IM as a drive motor in EV is an active area of research. IM is widely used in the industry for various applications, and several efficient IM control schemes are available in [7]. Despite such advantages, an IM has some drawbacks, like lower efficiency and higher volume, in contrast to the PMSM when applied to the EV. This is the driving force for researchers to develop IM-based powertrains at a higher power density. In the EV, the operating voltage of the drive motor is preferred to be low (in the range of 24–96 V) to meet electrical safety and battery power management requirements. The volume of the IM at low operating voltages increases with power capacity, as they require thick stator winding conductors. This can be addressed to some extent by using an open-end winding IM (OEWIM). The dc bus requirement of the OEWIM is only half that of the traditional IM to produce the same torque [7]. Because of this, the volume of an OEWIM is less than that of a traditional IM of the same power rating [8]. An OEWIM EV powertrain presented in [9] and [10] has two identical isolated battery packs (BP) that power two two-level (2L) voltage source inverter (VSI) connected to the OEWIM. Dual 2L-VSI-fed OEWIM resembles the three-level operation with reduced switching power losses, improved harmonic characteristics, and reduced torque ripple. This configuration with isolated BPs has better reliability due to its fault-tolerant operation (FTO). The VSI used in the EV may fail due to switch failure, malfunctioning of gate drivers, low charge in the battery, and mechanical vibration. Moreover, one BP [either battery pack-1 (BP1) or battery pack-2 (BP2)] may have a low charge to feed the VSI. Owing to the inherent FTO of the VSI-fed OEWIM, it can be operated as a traditional IM drive when one VSI or one BP goes into inoperative mode. During the FTO of the OEWIM, the same maximum torque can be obtained as that of the healthy condition [11], [12].

The performances of the EV with different drive train arrangements such as all-wheel drive (AWD), four-wheel drive (4WD), front-wheel drive (FWD), rear-wheel drive (RWD), and differential four-wheel drive (D4WD) are investigated in [12], [13], [14], [15], and [16]. Despite the satisfactory performance of FWD and RWD, they lack FTO. 4WD and AWD are both superior in terms of performance. Each wheel is individually controlled by two motor drives to achieve FTO [15]. Due to the need for individual control for each wheel, the control algorithms during FTO become complicated in the case of 4WD and AWD. In the D4WD mechanism, the drive power is transmitted to a pair of front and rear wheels through a transmission shaft, and the wheels are allowed to rotate at different speeds during turning [12]. Due to such features, the stability of the vehicle with the D4WD arrangement is better during turning and forward acceleration operation. Furthermore, FWD and RWD operation can be achieved in the vehicle with D4WD arrangement when one of the drive motors fails. Therefore, the D4WD arrangement with two OEWIM drives is used in this research work, as shown in Fig. 1.

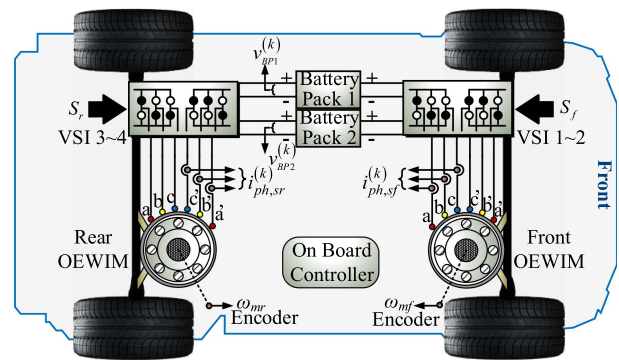


Fig. 1. OEWIM-based D4WD for the EV.

Direct torque control (DTC) has a fast dynamic torque response. In addition, DTC has less computational burden since decoupling and transformation of variables are not required [17], [18], [19], [20]. A D4WD EV powertrain with DTC-operated dual OEWIM propulsion is powered by two isolated BPs [12]. However, in this scheme, the load sharing by such BPs is unequal due to the unequal charging level, different charging profiles, unequal internal resistances of the batteries, manufacturing differences, and external weather conditions [21]. The discharge current of the weaker BP is higher than that of the healthy BP, and the weaker battery will further degrade. To achieve better EV performance, both BPs need to be loaded proportionally and should deliver power at an equal voltage level. Although various control schemes are studied in the literature to control the motor drive of EVs, few of them have investigated the drive control and the battery state-of-charge (SoC) control together [9]. Considering the aforementioned literature reviews, the following are some of the concerns that need to be solved for the dual OEWIM driven D4WD drive supplied by an isolated power supply.

- 1) During power sharing between the BP and VSI, there is a possibility of a mismatch in the SoC of the batteries. To some extent, these issues are solved in [22], [23], [24], [25], [26], and [27]. However, these solutions are not directly related to the dual-motor drives application.
- 2) With the use of several high-performance controllers, such as model predictive control and field-oriented control, together with the SoC controller, it is possible to use a high-performance microcontroller, which is involved in complex calculations resulting in higher sampling frequencies. Consequently, the drive switching frequency is limited with a higher ripple content in torque and stator current, resulting in reduced performance. In this case, it is necessary to simultaneously control the SoC and the drive with a reduced computational burden by adopting the DTC scheme.

In [9], an attempt has been made to control the SoC of the battery and drive simultaneously to ensure equal power sharing of two BPs at the same voltage level. Redundant switching states of the two 2L-VSIs are carefully adopted to realize such a simultaneous control. The contributions of this article can be summarized as follows.

- 1) An improved power sharing control scheme is introduced to distribute the total power demand of the EV proportionally between two BPs with equal voltage levels during normal running conditions.
- 2) The torque and speed demand of the EV are smoothly distributed between RM and FM by adopting an optimization technique. As a result, a better dynamic performance of the D4WD EV is achieved during the HFET and FTP75 driving cycle tests.
- 3) With proper analysis for predefined hysteresis bands, a lookup table (LUT)-based DTC (LUT-DTC) is proposed with seven-level torque hysteresis controller. The same LUT can be utilized for both normal and fault-tolerant operation, provided that the fault index parameter is considered.
- 4) Using redundant voltage vectors, a secondary LUT is allocated to the SoC control based on the selected voltage group from the primary LUT.

A brief description of the dual OEWM-based D4WD EV topology is given in Section II. Section III focuses on DTC control and SoC management algorithms. Section IV presents the simulation and experimental results. Finally, Section V concludes this article.

II. PROPOSED DUAL OEWM POWERED D4WD EV

A. Topology Description

Fig. 1 depicts a configurable dual OEWM drive system for a differential four-wheel drive (D4WD) EV with two isolated battery banks. Two driving motors with specific speed–torque characteristics are used for the failsafe operation of the EV. Electric power is provided to FM and RM through four conventional three-phase two-level VSIs. For each motor, there are two sets of VSIs: one is connected to BP1, while the other is connected to BP2, as shown in Fig. 1. These two isolated BPs are connected in a way that avoids circulating current within it and maintains its voltage level at $V_{dc}/2$ such that $V_{BP1} = V_{BP2}$.

The modeling of each VSIs is provided in Section II-B. Taking into account V_{BP1} and V_{BP2} at different voltage levels, a power splitting method is described in Section II-C. This power splitting approach is utilized to investigate the power flow within VSIs and helps to understand the power requirements of BPs. This also describes the power flow relations for both OEWMs. A necessary and accurate modeling of both FM and RM is developed in Section II-D to achieve proper drive control, as mentioned in Section III.

B. Modeling of Drive Inverters

Dual 2L-VSI has six legs, and each leg has two switches with complementary states of “1” or “0.” To effectively drive the switches, six different switching functions are developed, namely $S_l \in \{S_{al}^{(k)}, S_{bl}^{(k)}, S_{cl}^{(k)}, S_{a'l}^{(k)}, S_{b'l}^{(k)}, S_{c'l}^{(k)}\}$. Here, the subscript l (f : front and r : rear) is used to express the EV variables and k denotes the present sample of the DSP controller with sampling time T_s . Each switching function is selected according to Fig. 2(a) and (b). Using these switching functions along with the measured dc-link battery voltages ($V_{BP1}^{(k)}$ and $V_{BP2}^{(k)}$), the phase voltage across each winding of the FM and

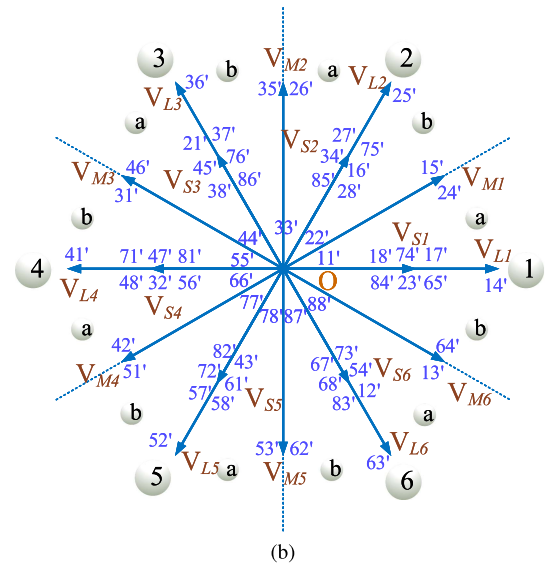
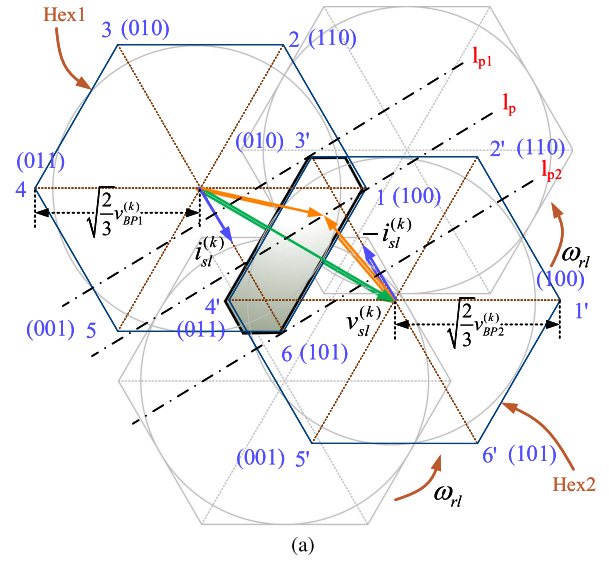


Fig. 2. (a) Power sharing between the inverters connected to FM and RM. (b) Possible VVs for the dual VSI-fed OEWM drive.

RM can be evaluated as (1) [12]. This process reduces the usage of the number of voltage sensors to two.

$$\begin{bmatrix} v_{aa'l}^{(k)} \\ v_{bb'l}^{(k)} \\ v_{cc'l}^{(k)} \end{bmatrix} = \begin{bmatrix} S_{al}^{(k)} \\ S_{bl}^{(k)} \\ S_{cl}^{(k)} \end{bmatrix} V_{BP1}^{(k)} - \begin{bmatrix} S_{a'l}^{(k)} \\ S_{b'l}^{(k)} \\ S_{c'l}^{(k)} \end{bmatrix} V_{BP2}^{(k)}, \quad l \in \{f, r\} \quad (1)$$

where $\{v_{aa'l}^{(k)}, v_{bb'l}^{(k)}, v_{cc'l}^{(k)}\}$ denote the phase voltages across stator windings, i.e., $ph \in \{aa', bb', cc'\}$. The dual 2L-VSI fed OEWM drive has 64 (2^6) potential switching states, as demonstrated in Fig. 2(b). These switching states each have voltage vectors (VV) that can be characterized as being large (6), medium (12), small (36), or zero (10) vectors. If the switching state 25' (V_{L2} , i.e., large vector) will be selected, it can be formed by two individual 2L-VSI switching states $V_2(110) - V_5'(001)$, as shown in Fig. 2(a). Out of these 64 VVs, totally 34 VVs (large: 6, medium: 12, small: 12, and zero: 4) can be utilized for fault-free operation of the proposed DTC drive. The design

of numerous performance indices is possible because of the use of redundant small and medium VVs. This especially applies to small vectors, which can lead to a reduction in switching loss, fault tolerance, and SoC balancing. Twelve suitable small VVs (23,' 65,' 34,' 16,' 45,' 21,' 56,' 32,' 61,' 43,' 12,' 54') are considered here for normal operation. When an inverter connected to OEWM fails, the rest of the 24 small VVs are utilized out of the 36 small VVs. During failure operation, large and medium VVs are not utilized. Four zero VVs (78,' 88,' 87,' 77') are being utilized during both normal and faulty operations.

C. Dual OEWM Power Sharing Analysis

To make optimum use of battery power, all the operational range of an EV must be considered. As a result, the power flow of the proposed configuration could be the deciding factor. The OEWM and its connected differential must be able to drive the vehicle at its maximum speed during full torque generation. No matter how much battery power is available, the utilization of dual OEWM depends on the peak power demand of the EV. This peak power demand can only be determined from the maximum speed and torque requirement of the EV. It is possible to determine the stator power of FM (P_{sf}) and RM (P_{sr}) simultaneously using the following equation in steady state:

$$P_{sl} = \underbrace{R_{sl} \left[(i_{sl}^\alpha)^2 + (i_{sl}^\beta)^2 \right]}_{\text{Copper Loss}} + \underbrace{\frac{\omega_{rl}}{p_l} T_{ml}}_{\text{Shaft Power}}, \quad l \in \{f, r\} \quad (2)$$

where p_l denotes the number of pole pairs. i_{sl} ($= i_{sl}^\alpha + j i_{sl}^\beta$) is the current space vector of the stator in the $\alpha\beta$ plane and can be obtained according to (7). It is concluded from (2) that the speed and torque distribution of the EV affects the entire shaft power distribution. The FM/RM speed and torque distribution are discussed in Section III-A to validate this investigation. The FM/RM speed distribution factor depends on the factor $\cos \delta$ according to (9) and the FM/RM torque distribution can be made according to (10) considering the torque distribution factor W . As the OEWM power is directly proportional to the torque requirement, the distribution factor W can also be utilized to balance the power requirements of the two OEWMs. In other words, W can be used to distinguish the power flow from BPs, since the EV is powered by two BPs. For the sake of argument, let us say I^* is the total current demand by EV and $i_1 \dots i_4$ are the battery current entering VSI1 \sim 4 from BP1 and BP2. In other words, the total amount of FM (i_{FM}) and RM (i_{RM}) current required can be expressed as (3).

$$i_{FM} = i_1 + i_2 = W I^*, \quad i_{RM} = i_3 + i_4 = (1 - W) I^*. \quad (3)$$

Again, the current drawn from BP1 (i_{BP1}) and BP2 (i_{BP2}) can be deduced as follows:

$$i_{BP1} = i_1 + i_4 = f_{BP1}(W), \quad i_{BP2} = i_2 + i_3 = f_{BP2}(W) \quad (4)$$

where $f_{BP1}(W)$ and $f_{BP2}(W)$ are the function of BP1 and BP2 current and depend on the factor W . While the vehicle accelerates, the rear motor is more loaded, and therefore, W becomes smaller (i.e., $0 < W < 0.5$). On the contrary, FM is loaded more during retardation, so W becomes larger (i.e., $0.5 < W < 1$).

The variable W is completely dependent on the longitudinal force distribution; therefore, it depends on the torque distribution relations in (10). The proposed LUT-DTC scheme in Section II-B utilizes an SoC balancing scheme through VVs arrangement and indirectly equalizes i_{BP1} and i_{BP2} (i.e., $i_{BP1} \approx i_{BP2}$) under nearly equal battery pack voltages.

Fig. 2(a) shows a power splitting approach for individual inverters connected to FM or RM in a $\alpha\beta$ -plane. Unequal voltage levels (V_{BP1} , V_{BP2}) are considered for a better understanding of power sharing behavior. Hex1 (Hex2) indicates the hexagons in Fig. 2(a) formed by VSI1 and VSI4 (VSI2 and VSI3) VVs. The intersection of Hex1 and Hex2 provides a shaded polygon region that corresponds to the feasible power-sharing limit of the dual inverter-fed OEWM drives. The shaded polygon limits to only part of the hexagon or covers the whole hexagon, depending on the battery voltage level and appropriate modulation range. l_p shows the locus of power shared by VSI-1 (VSI-4) and VSI-2 (VSI-3) in FM (RM) operation. The locus l_{p1} indicates the minimum power shared by VSI-1 (VSI-4) and the maximum power shared by VSI-2 (VSI-3). Similarly, the locus l_{p2} indicates the maximum power shared by VSI-1 (VSI-4) and the minimum power shared by VSI-2 (VSI-3).

D. OEWM Reference Model

The OEWM model discussed here is analyzed in the two-phase power-invariant $\alpha\beta$ (stationary) reference frame as (5). A generic variable X represents a space vector corresponding to voltage (v), current (i), and flux (ψ).

$$X_{sl}^{(k)} = \sqrt{\frac{2}{3}} \sum_{n=1, l \in \{f, r\}}^3 X_{ph,sl}^{(k)} e^{j \frac{2\pi(n-1)}{3}} \quad (5)$$

where $ph \in \{aa', bb', cc'\}$ are the phases corresponding to each winding of the OEWM. The term m represents the number of phases, and the subscripts $\{s, r\}$ denote the stator and rotor, respectively.

For analyzing the drive motor performance, a suitable discrete-time modeling is essential, where a one-step delay is needed for smooth operation of the digital controller. The discrete-time model of the OEWM can be obtained as (6)–(8), utilizing the backward Euler approximation (i.e., $d\psi/dt = (\psi^{(k)} - \psi^{(k-1)})/T_s$). Here, a sampling interval of $T_s = 10 \mu s$ is considered for accurate modeling.

$$\begin{bmatrix} \psi_{sl}^{(k)} \\ \psi_{rl}^{(k)} \end{bmatrix} = \left(I + A_l^{(k-1)} T_s \right) \begin{bmatrix} \psi_{sl}^{(k-1)} \\ \psi_{rl}^{(k-1)} \end{bmatrix} + T_s \begin{bmatrix} v_{sl}^{(k-1)} \\ 0 \end{bmatrix} \quad (6)$$

$$\begin{bmatrix} i_{sl}^{(k)} \\ i_{rl}^{(k)} \end{bmatrix} = C_l \begin{bmatrix} \psi_{sl}^{(k)} \\ \psi_{rl}^{(k)} \end{bmatrix} \quad (7)$$

$$\omega_{rl}^{(k)} = \omega_{rl}^{(k-1)} + \frac{p_l T_s}{J_l} \left(T_{ml}^{(k)} - T_{Ll}^{(k)} \right) \quad (8)$$

$$A_l^{(k-1)} = \begin{bmatrix} 1 & \kappa_{rl} \\ \frac{\sigma_l \tau_{sl}}{\kappa_{sl}} & \frac{\sigma_l \tau_{sl}}{\sigma_l \tau_{rl}} + j \omega_{rl}^{(k-1)} \end{bmatrix}, \quad C_l = \begin{bmatrix} 1 & \kappa_{rl} \\ \frac{\sigma_l L_{sl}}{\kappa_{sl}} & \frac{\sigma_l L_{sl}}{\sigma_l L_{rl}} \\ -\frac{\sigma_l L_{sl}}{\sigma_l L_{rl}} & 1 \end{bmatrix}$$

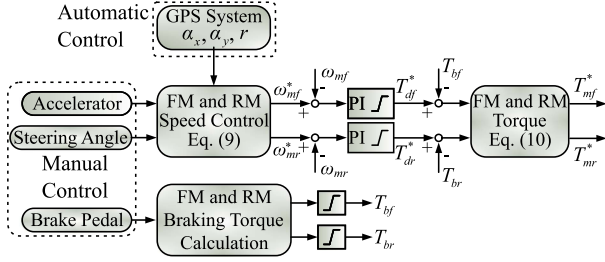


Fig. 3. Speed control and reference torque generation for FM and RM.

where $T_{ml}^{(k)} = \Im(p_l \hat{\psi}_{sl}^{(k)} i_{sl}^{(k)})$ and $T_{ml}^{(k)}$ are the electromagnetic torque developed and applied load torque by FM and RM. $\sigma_l = 1 - L_{ml}^2 / L_{sl} L_{rl}$ is the magnetizing coefficient; $\tau_{sl} = L_{sl} / R_{sl}$ and $\tau_{rl} = L_{rl} / R_{rl}$ are the stator and rotor time constants; $\kappa_{sl} = L_{ml} / L_{sl}$ and $\kappa_{rl} = L_{ml} / L_{rl}$ are the stator and rotor constants. J_l represents rotor moment of inertia. $\omega_{rl}^{(k)}$ is the rotor electrical speed of FM and RM at the k th instant.

III. OEWM DRIVE CONTROL WITH BATTERY SOC BALANCING USING THE PROPOSED LUT-DTC

Different torques can be used for every propulsion motor. Since each propulsion motor has different power conversion efficiency corresponding to each speed–torque characteristic, the appropriate torque splitting strategy can maximize the total efficiency of the propulsion motors. The introduction of the torque splitting technique in Section III-A significantly impacts the EV controller as an additional computational complexity. However, it is controlled separately and does not influence the power-splitting algorithm discussed in Section II-C.

A. Reference Generation

The suggested EV controller has the option of manually or automatically generating the FM speed reference. EVs can be driven manually by pressing the accelerator pedal, brake pedal, and then, guiding the car in the direction of the driver's choice. However, global positioning systems (GPSs) are being considered for the autonomous EV drive system. ω_{mf}^* is determined by the GPS and the destination target [12]. The RM reference speed (ω_{mr}^*) is computed from ω_{mf}^* using (9), where the steering angle (δ) is calculated from the direction of the EV with respect to the direction of the global longitudinal.

$$\omega_{mr}^* = \omega_{mf}^* \cos \delta. \quad (9)$$

The instantaneous speed of FM (ω_{mf}) and RM (ω_{mr}) is quantified using two high resolution speed encoders as a means of providing feedback to the speed controller. ω_{mf} (ω_{mr}) is compared with ω_{mf}^* (ω_{mr}^*), and then, passes through the proportional integral (PI) controller to regulate speed error, as shown in Fig. 3. Subsequently, it produces driving torque references for FM (T_{df}^*) and RM (T_{dr}^*), respectively.

While accelerating and decelerating, the EV encounters numerous forcing components, including the vehicle's overall mass. To stabilize the EV at various operating conditions, these force components are distributed separately to the front and rear

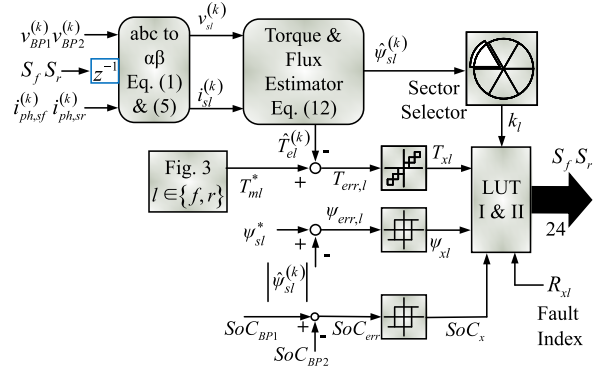


Fig. 4. LUT-DTC control structure for FM and RM, $l \in \{l, r\}$.

wheels/differentials. The longitudinal force required by the front differential is F_{xf} and the rear differential is F_{xr} , estimated at [12]. These forces combined with the wheel radius (R_w) produces the respective torque components. Let both FM and RM need a total torque of T^* to drive the EV. The optimal torque distribution between FM (T_{mf}^*) and RM (T_{mr}^*) can be determined by solving an unconstrained nonlinear optimization problem with an objective function mentioned in (10).

$$\begin{aligned} T_{mf}^* &= \min \{(T_{df}^* - T_{bf}^*), (R_w F_{xf})\} = W T^* \\ T_{mr}^* &= \min \{(T_{dr}^* - T_{br}^*), (R_w F_{xr})\} = (1 - W) T^* \end{aligned} \quad (10)$$

$$W = T_{mf}^* / (T_{mf}^* + T_{mr}^*) \quad (11)$$

where W denotes the torque distribution factor. T_{bl} ($l \in \{f, r\}$) is the braking torque produced by EV during deceleration or by applying the brake pedal.

B. LUT-DTC Methodology

The DTC technique is used to improve the efficiency and reliability of OEWM-driven EV systems under conditions such as motor parameter variability and inverter failure. An LUT-based DTC (LUT-DTC) technique is illustrated in Fig. 4 and is represented in a step manner as follows.

Step 1: Measure $v_{BP1}^{(k)}$, $v_{BP2}^{(k)}$, $i_{ph,sl}^{(k)}$, $i_{ph,sr}^{(k)}$, and ω_{ml} .

Step 2: Utilize the generated switching pulse S_l with a sample delay to produce $v_{sl}^{(k)}$ and $i_{sl}^{(k)}$ using (1) and (5).

Step 3: Compute the estimated stator flux ($\hat{\psi}_{sl} = |\hat{\psi}_{sl}^{(k)}| e^{j\hat{\rho}_{sl}^{(k)}}$) and the estimated torque $\hat{T}_{el}^{(k)}$ as per (12) for the front and back OEWM [12].

$$\begin{aligned} \hat{\psi}_{sl}^{(k)} &= \hat{\psi}_{sl}^{(k-1)} + T_{dtc} \left(\hat{v}_{sl}^{(k-1)} - R_{sl} \hat{i}_{sl}^{(k-1)} \right) \\ \hat{T}_{ml}^{(k)} &= \Im \left(p_l \hat{\psi}_{sl}^{(k)} \times \hat{i}_{sl}^{(k)} \right) \end{aligned} \quad (12)$$

where T_{dtc} is considered as DTC sample time and kept less than the controller sampling time T_s for better accuracy with a reduced switching frequency.

Step 4: Compare $\hat{T}_{el}^{(k)}$ and $|\hat{\psi}_{sl}^{(k)}|$ with the reference torque (T_{ml}^*) and the reference stator flux (ψ_{sl}^*) to generate the torque error $T_{err,l}$ and the flux error $\psi_{err,l}$. T_{ml}^* is computed from Fig. 3, while ψ_{sl}^* is computed from the speed-flux characteristics of FM and RM.

TABLE I

LUT I: DTC CONTROL LUT TO SELECT A VECTOR DURING OPERATION OF BOTH INVERTER AT BOTH HEALTHY AND FAULTY SITUATIONS

ψ_x	Sub Sector	T_x ($\{a_k, b_k\}$: Subsectors for q^{th} sector)						
		+3	+2	+1	0	-1	-2	-3
+1	a_k	$V_{L(k+1)}$	$V_{M(k)}$	$V_{S(k+1)}$	0	$V_{S(k+5)}$	$V_{M(k+4)}$	$V_{L(k+5)}$
	b_k	$V_{L(k+1)}$	$V_{M(k+1)}$	$V_{S(k+1)}$	0	$V_{S(k+5)}$	$V_{M(k+5)}$	$V_{L(k+5)}$
-1	a_k	$V_{L(k+2)}$	$V_{M(k+1)}$	$V_{S(k+2)}$	0	$V_{S(k+4)}$	$V_{M(k+3)}$	$V_{L(k+4)}$
	b_k	$V_{L(k+2)}$	$V_{M(k+2)}$	$V_{S(k+2)}$	0	$V_{S(k+4)}$	$V_{M(k+4)}$	$V_{L(k+4)}$

TABLE II

LUT II: PROPOSED DTC LUT FOR THE SELECTION OF VECTORS BASED ON SOC LEVEL TRANSITION

Sector (q)	SoC _x	$V_{S(k)}$		$V_{M(k)}$	
		+1	-1	+1	-1
Sector (q)	1	65'	23'	15'	24'
	2	16'	34'	26'	35'
	3	21'	45'	31'	46'
	4	32'	56'	42'	51'
	5	43'	61'	53'	62'
	6	54'	12'	64'	13'

Step 5: Generate the torque index T_{xl} from $T_{err,l}$ by utilizing a seven-level hysteresis comparator as in (13). The hysteresis comparator uses different levels of torque hysteresis band T_B , which can be estimated through offline analysis of the OEWM model presented in Section II-D [28].

$$T_{xl} = \begin{cases} +3 & \text{if } T_{err,l} \geq 0.7T_B \\ +2 & \text{if } 0.7T_B \geq T_{err,l} \geq 0.6T_B \\ +1 & \text{if } 0.6T_B \geq T_{err,l} \geq 0.3T_B \\ 0 & \text{if } 0.3T_B \geq T_{err,l} \geq -0.3T_B \\ -1 & \text{if } -0.3T_B \geq T_{err,l} \geq -0.6T_B \\ -2 & \text{if } -0.6T_B \geq T_{err,l} \geq -0.7T_B \\ -3 & \text{if } -0.7T_B \geq T_{err,l} \end{cases} \quad (13)$$

Step 6: Compute a flux index ψ_{xl} from $\psi_{err,l}$ using a two-level hysteresis controller as in (14). Similar offline analysis as in Step-5 can be utilized to identify the flux hysteresis band ψ_B .

$$\psi_{xl} = \begin{cases} +1 & \text{if } \psi_{err,l} \geq 0.5F_B \\ -1 & \text{if } -0.5F_B \geq \psi_{err,l} \end{cases} \quad (14)$$

Step 7: Obtain an appropriate VV group by utilizing T_{xl} , ψ_{xl} and the flux sector q in LUT-I, as shown in Table I. The flux sector can be obtained from the estimated stator flux angle $\hat{\rho}_{sl}^{(k)}$. To accurately measure the impact of VVs in each sector, all flux sectors are divided into two subsectors, namely a_q and b_q .

Step 8: Select the desired VV from LUT-II in Table II to balance the SoC of the BPs, whose details are provided in Section III-C.

Step 9: Generate the switching pulses S_i from the selected VVs as per Fig. 2(a).

The R_{sl} identification method requires a speed transient profile, where the motor performs a quick acceleration and deceleration operation at a wide range of speed variations. It is reported in [29] that the stator flux can be estimated accurately at higher speed without considering the drop corresponding to R_{sl} in (12). However, the need for R_{sl} can be realized for stator

flux estimation during low speed operation. At low speed, the variation in R_{sl} is quite negligible, i.e., around 1% of its rated value. The effect of this variation in R_{sl} does not have much impact on the system performance.

C. VVs Impact on SoC Balancing of BPs

When an EV is coupled to FM and RM drives, the DTC technique in [12] does not involve any relationship with the power flow from isolated battery packs. During transient and steady-state operations, the BPs draw unequal amounts of current. BPs with a higher current output may discharge faster as a result of additional stress than the other BPs at this time. Failure of the VSI attached to the discharged BP may also result in loss of full functionality of the OEWM in the EV. In these cases, the BPs SoC balance becomes even more critical. In this section, the interrelation between battery current and inverter power sharing through SoC balancing is thoroughly examined. The SoC is usually computed using the Coulomb counting approach, as in (15) to assess power sharing between BPs [30].

$$\text{SoC}_n = \text{SoC}_n^{(0)} - \frac{1}{C_n} \int i_n dt, \quad n \in \{\text{BP1}, \text{BP2}\} \quad (15)$$

where $\text{SoC}_n^{(0)}$ is the initial SoC concentration, C_n is the battery pack capacity, and i_n is the current demand of the battery pack. After comparing the battery pack SoC concentrations, a two-level hysteresis controller processes the error signal (SoC_{err}) to produce the SoC index (SoC_x) as in (16). SoC_x becomes “+1” when the SoC concentration of BP1 (SoC_{BP1}) is higher compared to the SoC concentration of BP2 (SoC_{BP2}). While the concentration of SoC_{BP2} surpasses that of SoC_{BP1} , SoC_x produces “-1.” The redundant VVs must be selected according to Table II that balances the SoC concentrations of both BPs in an interval T_{dtc} . It is reasonable to assume that $\hat{\psi}_{sl}$ is positioned at sector-1a with $T_{xl} = +1$ and $\psi_{xl} = +1$. According to Table I, a small vector has been picked for the time being. When considering $\text{SoC}_x = +1$, the VV 65' with a switching state of (101 – 001) is selected to reduce SoC_{BP1} . VV 23' (110 – 010) is selected on $\text{SoC}_x = -1$ that increases the concentration of BP1 SoC.

$$\text{SoC}_x = \begin{cases} +1, & \text{if } \text{SoC}_{BP1} \geq \text{SoC}_{BP2} \\ -1, & \text{if } \text{SoC}_{BP1} < \text{SoC}_{BP2} \end{cases} \quad (16)$$

The LUT-II mentioned in Table II corresponds to the SoC balancing by selecting the small- and medium-redundant VVs. Fig. 2(a) shows how the improved LUT-DTC algorithm chooses the preferred switching combination to monitor battery output power without the use of additional hardware. To prove the superiority of this approach, it is first simulated, and then, validated using an experimental prototype in the next section.

D. VVs Impact on Fault Tolerant Operation

Several failure cases are listed in Table III: single VSI failure or complete failure of either front or rear drive. The LUT-I is configured in such a way that the proposed LUT-DTC can be applicable for normal and failure operations, considering the fault index (R_{xl}). R_{xl} is set to 0 or 1 for normal operation or at the occurrence of the fault, respectively. Consequently,

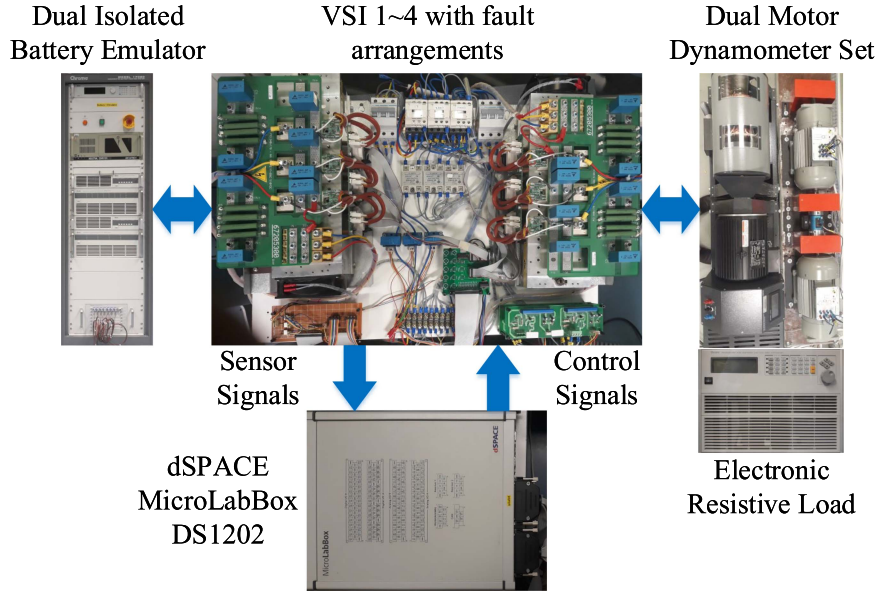


Fig. 5. Experimental prototype for the dual OEIWM D4WD EV.

TABLE III
OEIWM CURRENT CONCERNING BATTERY CURRENT
UNDER INVERTER FAILURE

Failed VSI	i_{FM}	i_{RM}
VSI-1	$i_2 = WI^*$	$i_3 + i_4 = (1 - W)I^*$
VSI-2	$i_1 = WI^*$	$i_3 + i_4 = (1 - W)I^*$
VSI-3	$i_1 + i_2 = WI^*$	$i_4 = (1 - W)I^*$
VSI-4	$i_1 + i_2 = WI^*$	$i_3 = (1 - W)I^*$
VSI-1 and VSI-2	0	$i_{RM} = i_3 + i_4 = I^*$
VSI-3 and VSI-4	$i_1 + i_2 = I^*$	0

suitable VVs can be selected according to the FTO mentioned in [12]. However, only LUT-II can be applicable during normal operation. Under failure of VSI-1 (or VSI-2), FM is configured as a single-ended IM, and therefore, powered by VSI-2 (or VSI-1) only. At this moment, only BP2 (or BP1) provides the overall current requirement of FM for the fail-safe operation of the EV, while RM is supplied from both battery packs. Likewise, with the failure of VSI-4 (or VSI-3), RM is configured as a single-ended IM, and thus, powered by VSI-3 (or VSI-4) only. At this time, BP2 (or BP1) provides the overall current required for RM for the fail-safe operation of the EV, while FM is supplied from both battery packs. For a single-ended FM or RM drive operation, only small VVs 71,' 72,' 73,' 74,' 75,' 76' (17,' 27,' 37,' 47,' 57,' 67') and zero VVs 77,' 78' (77,' 87') are used for driving VSI-2 or VSI-3 (VSI-1 or VSI-4). As the distribution factor W depends on the overall torque and speed distribution, the current distribution of FM and RM under FTO is expressed in Table III.

This analysis shows that under FTO, the power distribution among battery packs is unequal. The detailed analysis of the EV drive under FTO with the support of the current waveform of the battery pack is validated through the simulation and experimental results given in Section IV. This problem can be addressed by using a proper battery power management algorithm, which is

TABLE IV
EXPERIMENTAL PARAMETERS FOR D4WD EV

OEIWM experimental parameters	
$3\Phi, 415 \text{ V}, 5 \text{ kW}, 10.5 \text{ A}, 60 \text{ Hz}, 1740 \text{ r/min}, 0.87 \text{ PF}$	
$R_s = 0.8593 \Omega, R_r = 1.033 \Omega, L_{ls} = L_{lr} = 6.8 \text{ mH}$	
$l_m = 170.2 \text{ mH}, J = 0.038 \text{ kg}\cdot\text{m}^2, B = 0.001$	
Experimental VSI Specifications	
$V_{dc} = 600 \text{ V}, V_{ac, L-L} = 467 \text{ V}, I_{ac} = 50 \text{ A}$	
$P_{ac} = 35 \text{ kW}, P_{loss} = 0.01 P_{ac}, f_{sw} = 30 \text{ kHz}, \cos \phi = 0.87$	
Battery emulator specifications	
120 V, 100 A, 10 kW, Eff. > 90%, PF > 0.95, THD _i < 5%	
Experimental controller specifications	
$k_p = 3.46, k_i = 1.83, T_B = 1.23, \psi_B = 0.01, \text{SoC}_B = 100\%$	

beyond the scope of this article. When both the inverters VSI-1 and VSI-2 of FM drive (or VSI-3 and VSI-4 of RM) fail, the EV can operate as RWD (or FWD). Under these conditions, the battery packs are loaded equally as shown in Table III.

IV. RESULTS AND DISCUSSION

A. Hardware Setup Description

Initially, the D4WD EV drive system presented in Fig. 1 was verified using MATLAB/SIMULINK-based simulation. With satisfactory simulation performance, the experimental setup has been developed in the laboratory and the complete arrangement is shown in Fig. 5. The specifications of the VSIs and OEIWMs used in the experiment are listed in Table IV. In the designed prototype, two OEIWM with built-in dynamometer sets, four 2L-VSIs, and two isolated battery emulators are used. To measure three-phase stator currents, three sets of through-hole analog current transducers (LEM HAL-50S) are chosen. For an accurate measurement of both BP voltages, two analog isolation

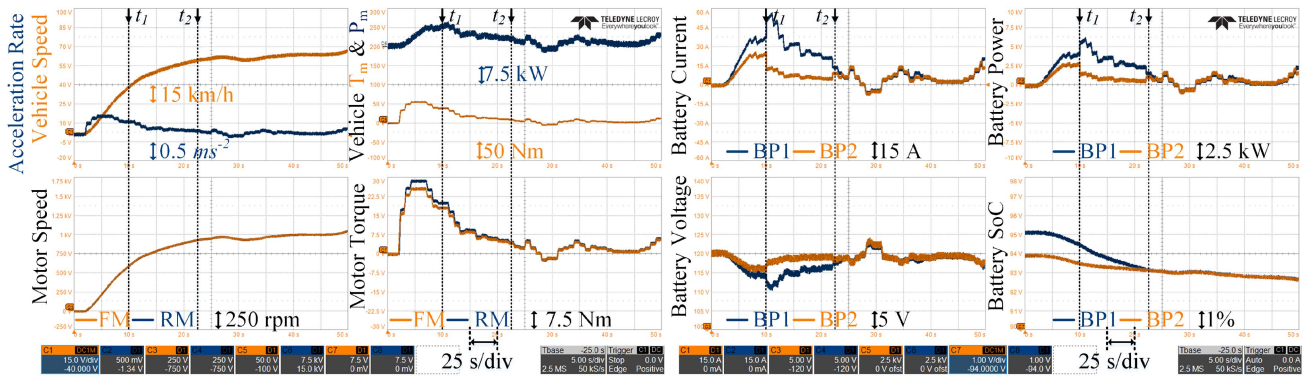


Fig. 6. Experimental results during acceleration.

amplifiers (AD215) are used. The placement of current and voltage sensors is depicted in Fig. 5. The analog signals from both voltage and current sensors are filtered before entering into the analog port of the real-time dSPACE MicroLabBox (DS1202) controller. Such a controller has an integrated analog-to-digital converter to convert those analog signals into the corresponding signals. The proposed modified DTC scheme, as presented in Fig. 4, is executed through this digital controller. The DS1202 controller is used to supply various control signals to four VSIs with 24 insulated-gate bipolar transistors via gate drivers and battery emulators. Optoisolators with sufficient bandwidth are employed to provide the required isolation. A fault detection algorithm is implemented to detect the VSI fault. Once the faulty VSI is detected, a relay-controlled double-pole single-throw switch can isolate the entire faulty VSI and short-circuit one end of either FM or RM. In addition, differences in the SoC of BPs can be detected by a comparator and trigger control activities.

B. Performance at Various Stages of Operation

The HFET and FTP75 driving cycles represent the standard driving cycle testing as seen in a practical system. Therefore, a portion of the FTP75 driving cycle is considered to test the SoC balancing capability of the proposed controller at various stages of operation, i.e., acceleration, running, turning, and deceleration of the vehicle. The experimental results validated for this test include motor speed, motor torque, EV power demand, acceleration and deceleration rate, battery voltage, battery current, battery power, and % SoC of BP.

1) During Acceleration: When the EV is accelerating, the effectiveness of the suggested DTC technique with closed-loop SoC control is demonstrated, and the related waveforms are plotted in Fig. 6. It has been discovered that the SoCs of the two battery packs are initially different, i.e., 95% for BP1 and 94% for BP2. The closed-loop control for SoC balancing is enabled at the time of activation $t = t_1$ s. To raise the SoC to the same level as before activation of the SoC control method, the current drawn from BP1 is proportionally larger than the current drawn from BP2. Finally, as a result of the controller action, the SoC of the BPs is balanced at $t = t_2$ s.

2) During Running: The effectiveness of the proposed DTC scheme with closed-loop SoC control is verified when the EV runs under normal road conditions. The corresponding

waveforms are plotted in Fig. 7, where both BPs with different SoC levels (95% for BP1 and 94% for BP2) are initially observed. The proposed controller is applied at $t = t_1$ s and achieved SoC balancing for the BPs at $t = t_2$ s.

3) During Turning: Utilizing the turning commands (both left and right turns), the effectiveness of the proposed DTC scheme on SoC balancing is verified. Fig. 8 shows the performance evaluation of the EV with turning conditions. It is observed that when the EV takes turns, the RM moves at a slower speed than the FM. This speed depends on the steering angle. SoC control action is enabled at $t = t_1$ s while the EV turns right. The controller allows BP1 to deliver a higher current than BP2 to bring the SoC of both BPs to the same level. As a result of such control action, the SoC of the BPs is balanced at $t = t_2$ s. At the same time, the performance of the LUT-DTC scheme is satisfactory in terms of torque control.

4) During Deceleration: When the speed of a running EV is required to be decreased, the brake pedal is subjected to a force. With the break command, the EV speed decreases and both OEWM operate in a regenerative mode. In other words, both OEWMs run as a generator during this period and feed the electrical energy back to the BPs, which are being used to charge them. At the beginning of the deceleration mode, the SoC of BP1 and BP2 was maintained at 91% and 90.4%, respectively, as shown in Fig. 9. At $t = t_1$ s, the SoC control loop is activated, and the controller allows BP2 to be charged at a faster rate than BP1. After a few seconds at $t = t_2$ s, the SoC of both BPs is balanced. The SoC control loop not only regulates the SoC level of both BPs, but also in a timely manner so that the EV can run with a properly balanced SoC during its next run.

C. Performance of Driving Cycle Testing

The performance of the D4WD EV prototype is tested for HFET and FTP75 driving cycles, as shown in Figs. 10 and 11. The required experimental test is performed to verify the efficacy of the proposed LUT-DTC with an SoC controller. With the suggested controller, BPs can be charged and discharged simultaneously (during regeneration). Both battery emulators (BP1 and BP2) have their SoC levels set to 97% and 95% before the experiment begins. This 2% SoC disparity is purposely kept, ensuring the effectiveness of the proposed controller's control action. The power-sharing algorithm first detects this

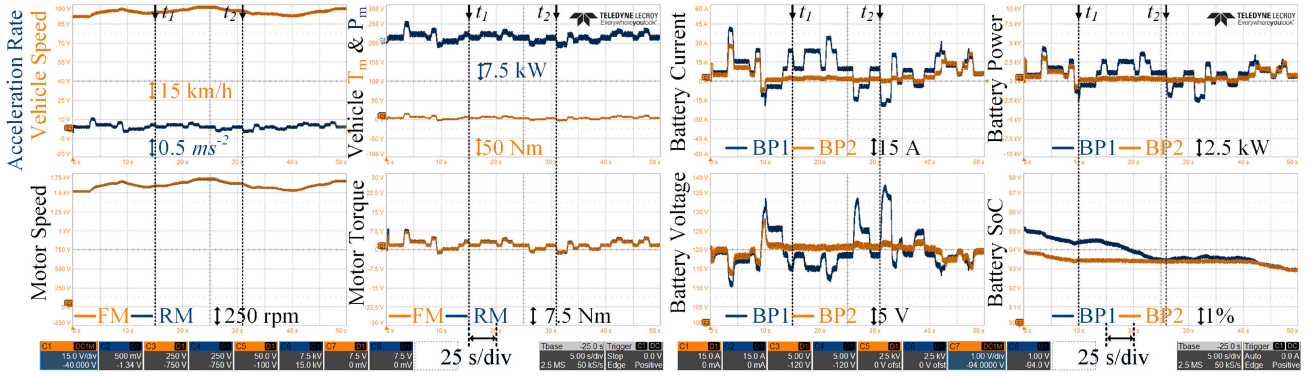


Fig. 7. Experimental results during normal running.

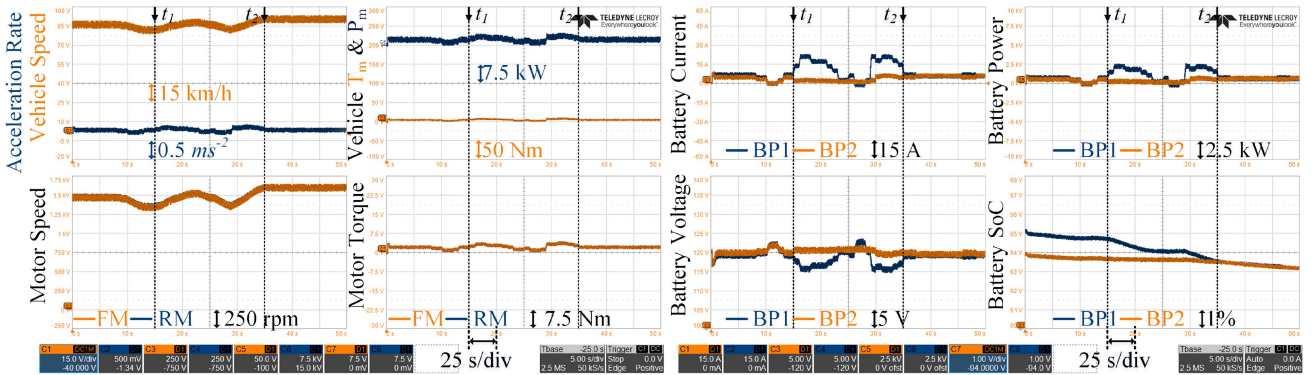


Fig. 8. Experimental results during turning.

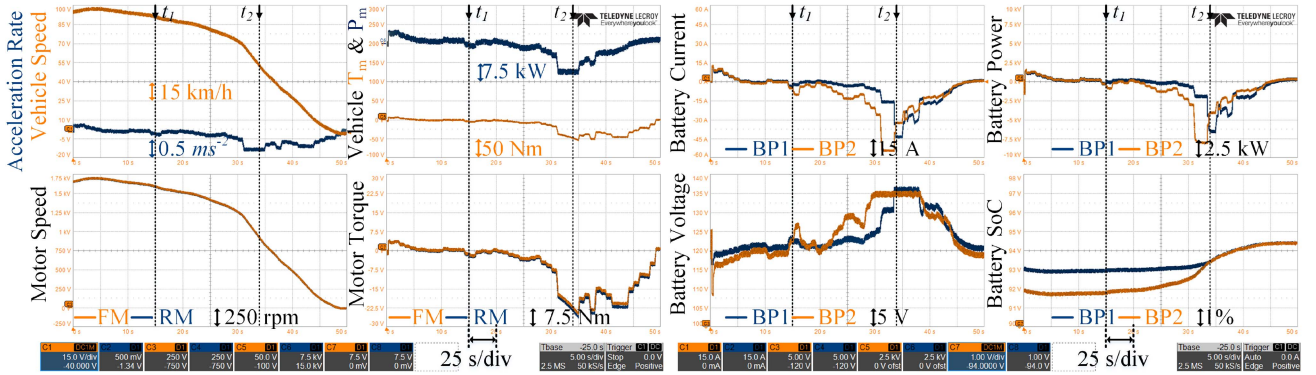


Fig. 9. Experimental results during deceleration.

discrepancy in the SoC level when the experiment is started. The VVs for VSI-2 and VSI-3 are chosen so that their output voltage magnitudes are greater than those for VSI-1 and VSI-4, respectively. During this period, VSI-1 and VSI-4 draw more current to balance the voltage level; therefore, the discharge rate of BP1 is significantly higher than that of BP2. This means that the initial discrepancy in the SoC level gradually decreases and the SoC of the BPs is well balanced at $t = t_1$. The same voltage vectors are then applied to all VSIs, allowing both BPs to produce power while maintaining the same SoC. The D4WD EV is experimented with FTP75 and HEFT driving cycles to see if the proposed controller works as mentioned.

D. Comparative Performance

The proposed LUT-DTC strategy is superior compared to MPDTC [31], considering the following.

- 1) By executing the algorithm on a digital controller dSPACE MicroLabBox DS1102 at a 150 MHz CPU frequency, the computational burdens are measured. The maximum sampling frequency of the drive system controller is kept at 40 kHz, so the time consumption of one control cycle should be less than $25 \mu\text{s}$. Fig. 12 shows the timing information between the proposed DTC scheme, MPDTC [31] and MPC [32]. It is observed that the proposed LUT-DTC utilizes less computational resources,

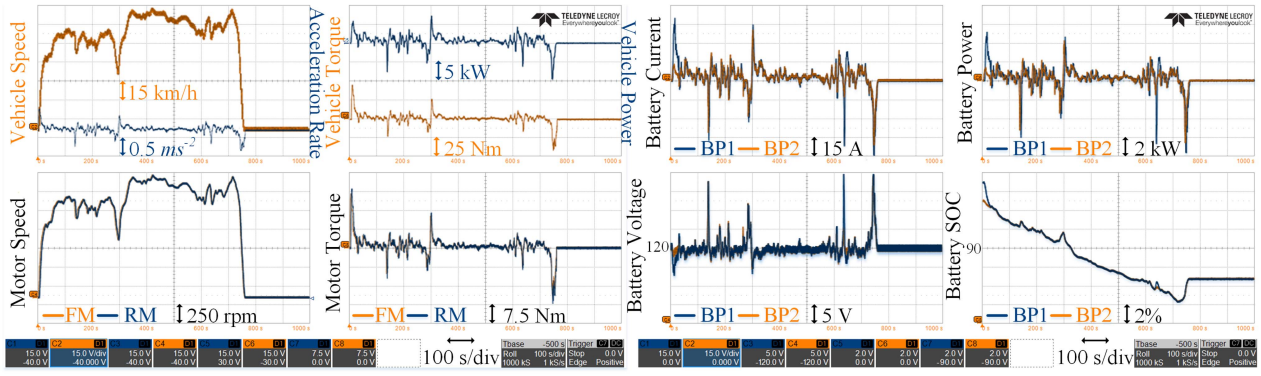


Fig. 10. Experimental results for HFET driving cycle testing.

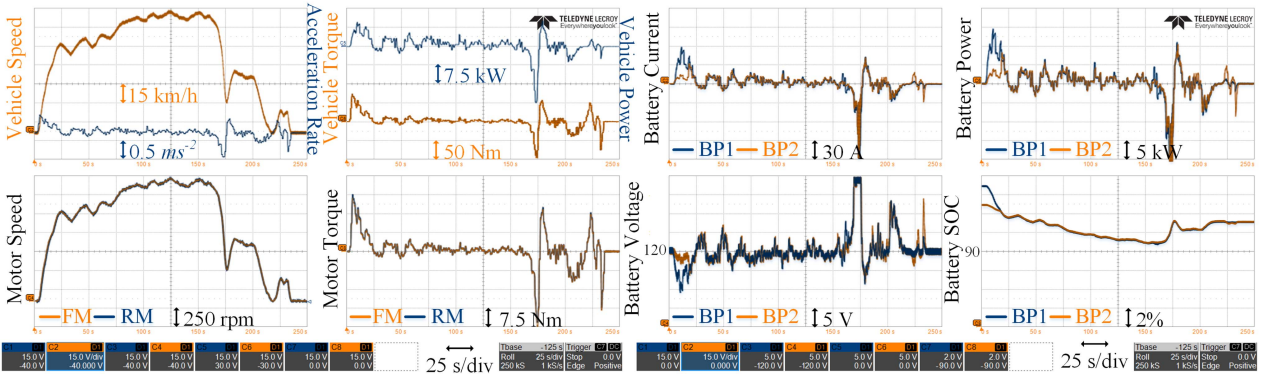


Fig. 11. Experimental results for FTP75 driving cycle testing.

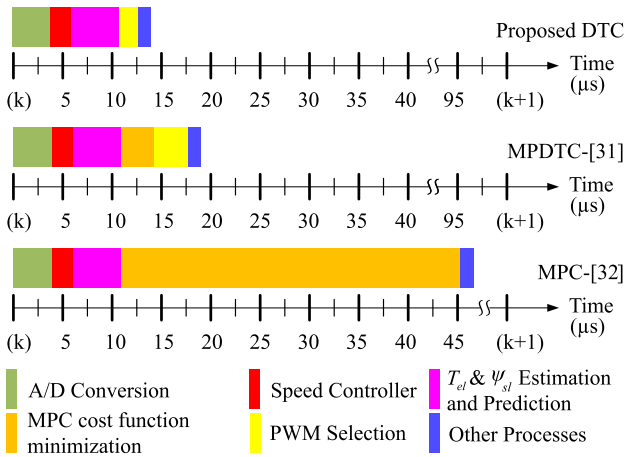


Fig. 12. Computational timing diagram of real-time implementation for proposed DTC scheme, MPDTC [31] and MPC [32].

whereas MPDTC[31] and MPC[32] are relatively more complex in calculating the optimum voltage vector to be used.

- 2) The proposed LUT-DTC depends solely on the stator resistance (R_{s1}) during drive operation. At higher speeds, the impact of the voltage drop corresponding to R_{s1} is negligible. Voltage drops across R_{s1} have substantial effects on flux estimation at lower speeds, and therefore, should

TABLE V

RIPPLE % COMPARISON FOR PROPOSED LUT-DTC AND MPDTC [31] FOR REAR MOTOR DURING (I) SCENARIO 1 (S-1: 300 R/MIN), (II) SCENARIO 2 (S-2: 600 R/MIN), AND (III) SCENARIO 3 (S-3: 1500 R/MIN)

Parameters (in %)	Proposed			MPDTC [31]			% Improvement		
	S-1	S-2	S-3	S-1	S-2	S-3	S-1	S-2	S-3
ΔT_{er}	2.46	3.37	2.34	3.32	4.54	3.64	25.9	25.8	35.7
$\Delta \omega_{mr}$	2.15	4.53	7.53	4.18	7.13	10.84	48.6	36.5	30.5
Δi_{sr}	3.57	7.46	5.67	8.26	9.43	8.24	56.8	20.9	31.2
ΔP_{sr}	1.45	2.36	2.72	2.56	4.78	8.26	43.4	50.6	67.1
Δi_{BP1}	6.67	8.28	10.52	8.03	10.63	12.39	16.9	22.1	15.1
η_{mr}	87.5	86.4	89.3	87.3	85.9	88.7	0.229	0.582	0.676

be included in the flux estimation process. As far as the variation in R_{s1} during OEWIM operation is concerned, it is very negligible, say $\approx 1\%$. However, the optimized VV compensates for the performance degradation resulting from such parameter variation. In MPDTC [31], the estimation of torque and flux components completely depends on the motor electrical parameter.

- 3) As far as the robustness of the control strategy is considered, the proposed LUT-DTC has a better dynamics than the MPDTC [31], as shown in Table V. This is because the proposed LUT-DTC utilizes the PI regulator and hysteresis controller, which acts very fast for the controlled input. The efficiency of the D4WD drive is better, i.e., 87.5~89.3 % during wide range of speed variations.

TABLE VI

PROPOSED D4WD LUT-DTC PERFORMANCE COMPARISON WITH OTHER CONTROL METHODOLOGY (M₁: OEWM, M₂: IM, M₃: OEWPMSM, M₄: PMSM, C₁: DTC, C₂: FOC, M₃: MPC, M₄: MPDTC)

Ref.	Motor Type	No. of Motor	Control Method	Circulating Current	SoC Balancing	Torque Ripple (%)	Current THD (%)	Efficiency (%)
[11]	M ₁	1	C ₁	Yes	No	11.2	8.23	84.4
[12]	M ₁	2	C ₁	No	Partial	2.46	5.67	89.3
[15]	M ₄	2	C ₂	Yes	Yes	<10	<8	>90
[16]	M ₄	4	C ₃	Yes	No	<10	<7	>90
[17]	M ₁	1	C ₁	Yes	No	10.8	9.26	86.8
[18]	M ₂	1	C ₁	Yes	No	8.36	4.78	86.32
[19]	M ₃	1	C ₃	Yes	No	4.92	3.27	91.5
[20]	M ₁	1	C ₄	Yes	No	8.29	7.56	87.3
[31]	M ₁	2	C ₄	No	Yes	3.64	8.24	88.7
Proposed	M ₁	2	C ₁	No	Yes	2.34	3.57	89.3

Again, the proposed LUT-DTC performance is compared with the different scheme presented in [11], [12], [15], [16], [17], [18], [19], [20], and [31], and the various performance parameters are shown in Table VI. It is observed that the proposed LUT-DTC is better with various performance support such as SoC, circulating current with reduced torque and current ripple. The efficiency of the OEWM-based D4WD is better than that of the IM drives when using the proposed LUT-DTC, as shown in Tables V and VI.

V. CONCLUSION

A dual OEWM-based differential four-wheel DTC drive for EV with SoC control was presented in this article. To achieve a proper power flow management between FM and RM, a suitable speed and torque distribution scheme was established. An improved two-stage LUT-DTC technique was proposed for the SoC control of battery packs. The proposed LUT-DTC with VV analysis had faster dynamics and improved speed and torque performance. The EV was tested under various operating conditions such as acceleration, deceleration, turning, and normal running to verify the performance of SoC balancing. The performance of the dual OEWM-based D4WD EV was evaluated using FTP75 and HEFT driving cycles. The proposed method was tested during inverter failure to demonstrate fault-tolerant operation. The proposed drive was shown to have an excellent dynamic performance and battery SoC control under normal and fault conditions. With the FTO operation, the proposed drive will find applications in heavy-duty ground EVs, as well as ship and aircraft electric propulsion systems. With the proposed LUT-DTC and dual motor driven D4WD, 89.2% efficiency was achieved. The future challenge will be to study the performance of the proposed controller in vehicle-to-grid, grid-to-vehicle, and vehicle-to-vehicle power flow.

REFERENCES

- [1] A. Salem and M. Narimani, "A review on multiphase drives for automotive traction applications," *IEEE Trans. Transport. Electrific.*, vol. 5, no. 4, pp. 1329–1348, Dec. 2019.
- [2] P. Ramesh and N. C. Lenin, "High power density electrical machines for electric vehicles—Comprehensive review based on material technology," *IEEE Trans. Magn.*, vol. 55, no. 11, pp. 1–21, Nov. 2019.
- [3] R. Deng, Y. Liu, W. Chen, and H. Liang, "A survey on electric buses—Energy storage, power management, and charging scheduling," *IEEE Trans. Intell. Transp. Syst.*, vol. 22, no. 1, pp. 9–22, Jan. 2021.
- [4] R. J. Javid and A. Nejat, "A comprehensive model of regional electric vehicle adoption and penetration," *Transport Policy*, vol. 54, pp. 30–42, Feb. 2017.
- [5] S. Hardman, "Understanding the impact of reoccurring and non-financial incentives on plug-in electric vehicle adoption—A review," *Transp. Res. A, Policy Pract.*, vol. 119, pp. 1–14, Jan. 2019.
- [6] H. Wang et al., "PLL- and FLL-based speed estimation schemes for speed-sensorless control of induction motor drives: Review and new attempts," *IEEE Trans. Power Electron.*, vol. 37, no. 3, pp. 3334–3356, Mar. 2022.
- [7] S. Lakhimsetty, V. S. P. Satelli, R. S. Rathore, and V. T. Somasekhar, "Multilevel torque hysteresis-band based direct-torque control strategy for a three-level open-end winding induction motor drive for electric vehicle applications," *IEEE Trans. Emerg. Sel. Topics Power Electron.*, vol. 7, no. 3, pp. 1969–1981, Sep. 2019.
- [8] S. Srinivas and K. Ramachandra Sekhar, "Theoretical and experimental analysis for current in a dual-inverter-fed open-end winding induction motor drive with reduced switching PWM," *IEEE Trans. Ind. Electron.*, vol. 60, no. 10, pp. 4318–4328, Oct. 2013.
- [9] U. R. Muduli et al., "An improved direct torque control with battery power management of open-end winding induction motor drive for electric vehicles," in *Proc. IEEE Energy Convers. Congr. Expo.*, 2020, pp. 6332–6337.
- [10] U. R. Muduli et al., "Predictive control based battery power sharing for four-wheel drive electric vehicle," in *Proc. IEEE Appl. Power Electron. Conf. Expo.*, 2021, pp. 817–821.
- [11] R. E. Kodumur Meesala and V. K. Thippiripati, "An improved direct torque control of three-level dual inverter fed open-ended winding induction motor drive based on modified look-up table," *IEEE Trans. Power Electron.*, vol. 35, no. 4, pp. 3906–3917, Apr. 2020.
- [12] U. R. Muduli et al., "Interrupt-free operation of dual-motor four-wheel drive electric vehicle under inverter failure," *IEEE Trans. Transport. Electrific.*, vol. 7, no. 1, pp. 329–338, Mar. 2021.
- [13] N. Mutoh and Y. Nakano, "Dynamics of front-and-rear-wheel-independent-drive-type electric vehicles at the time of failure," *IEEE Trans. Ind. Electron.*, vol. 59, no. 3, pp. 1488–1499, Mar. 2012.
- [14] N. Mutoh, "Driving and braking torque distribution methods for front-and-rear-wheel-independent drive-type electric vehicles on roads with low friction coefficient," *IEEE Trans. Ind. Electron.*, vol. 59, no. 10, pp. 3919–3933, Oct. 2012.
- [15] X. Hu, Y. Li, C. Lv, and Y. Liu, "Optimal energy management and sizing of a dual motor-driven electric powertrain," *IEEE Trans. Power Electron.*, vol. 34, no. 8, pp. 7489–7501, Aug. 2019.
- [16] H. Peng et al., "Torque coordinated control of four in-wheel motor independent-drive vehicles with consideration of the safety and economy," *IEEE Trans. Veh. Technol.*, vol. 68, no. 10, pp. 9604–9618, Oct. 2019.
- [17] B. R. Vinod, M. R. Baiju, and G. Shiny, "Five-level inverter-fed space vector based direct torque control of open-end winding induction motor drive," *IEEE Trans. Energy Convers.*, vol. 33, no. 3, pp. 1392–1401, Sep. 2018.
- [18] S. Suresh and R. P. P., "Virtual space vector-based direct torque control schemes for induction motor drives," *IEEE Trans. Ind. Appl.*, vol. 56, no. 3, pp. 2719–2728, May/Jun. 2020.
- [19] Y. Zhou et al., "An accurate torque output method for open-end winding permanent magnet synchronous motors drives," *IEEE Trans. Energy Convers.*, vol. 36, no. 4, pp. 3470–3480, Dec. 2021.
- [20] K. Eshwar and V. K. Thippiripati, "Weighting-factorless predictive torque control scheme for dual inverter fed open-end-winding PMSM with single DC source," *IEEE Trans. Power Electron.*, vol. 36, no. 11, pp. 12968–12978, Nov. 2021.
- [21] O. N. Nezamuddin, C. L. Nicholas, and E. C. d. Santos, "The problem of electric vehicle charging: State-of-the-art and an innovative solution," *IEEE Trans. Intell. Transp. Syst.*, vol. 23, no. 5, pp. 4663–4673, May 2022.
- [22] S. Xie et al., "Model predictive energy management for plug-in hybrid electric vehicles considering optimal battery depth of discharge," *Energy*, vol. 173, pp. 667–678, 2019.
- [23] P. Li, X. Jiao, and Y. Li, "Adaptive real-time energy management control strategy based on fuzzy inference system for plug-in hybrid electric vehicles," *Control Eng. Pract.*, vol. 107, 2021, Art. no. 104703.
- [24] S. F. da Silva et al., "Dual HESS electric vehicle powertrain design and fuzzy control based on multi-objective optimization to increase driving range and battery life cycle," *Appl. Energy*, vol. 324, 2022, Art. no. 119723.

- [25] X. Zhang et al., "Bi-level energy management of plug-in hybrid electric vehicles for fuel economy and battery lifetime with intelligent state-of-charge reference," *J. Power Sources*, vol. 481, 2021, Art. no. 228798.
- [26] S. Hu, Z. Liang, W. Zhang, and X. He, "Research on the integration of hybrid energy storage system and dual three-phase PMSM drive in EV," *IEEE Trans. Ind. Electron.*, vol. 65, no. 8, pp. 6602–6611, Aug. 2018.
- [27] J. J. Eckert, L. C. de Alkmin, F. G. Silva, D. Dedini, and F. C. Corrêa, "Electric vehicle powertrain and fuzzy control multi-objective optimization, considering dual hybrid energy storage systems," *IEEE Trans. Veh. Technol.*, vol. 69, no. 4, pp. 3773–3782, Apr. 2020.
- [28] B. Chikondra, U. R. Muduli, and R. K. Behera, "An improved open-phase fault-tolerant DTC technique for five-phase induction motor drive based on virtual vectors assessment," *IEEE Trans. Ind. Electron.*, vol. 68, no. 6, pp. 4598–4609, Jun. 2021.
- [29] C. Lascau, I. Boldea, and F. Blaabjerg, "A modified direct torque control for induction motor sensorless drive," *IEEE Trans. Ind. Appl.*, vol. 36, no. 1, pp. 122–130, Jan./Feb. 2000.
- [30] X. Lu et al., "State-of-charge balance using adaptive droop control for distributed energy storage systems in DC microgrid applications," *IEEE Trans. Ind. Electron.*, vol. 61, no. 6, pp. 2804–2815, Jun. 2014.
- [31] U. R. Muduli et al., "Predictive control with battery power sharing scheme for dual open-end-winding induction motor based four-wheel drive electric vehicle," *IEEE Trans. Ind. Electron.*, vol. 69, no. 6, pp. 5557–5568, Jun. 2022.
- [32] R. E. Kodumur Meesala, V. P. K. Kuniseti, and V. Kumar Thippiripati, "Enhanced predictive torque control for open end winding induction motor drive without weighting factor assignment," *IEEE Trans. Power Electron.*, vol. 34, no. 1, pp. 503–513, Jan. 2019.



Utkal Ranjan Muduli (Senior Member, IEEE) received the B.Tech. degree in electrical and electronics engineering from the Biju Patnaik University of Technology, Rourkela, India, in 2011, the M.Tech. degree in electrical engineering from the Indian Institute of Technology, Gandhinagar, India, in 2014, and the Ph.D. degree in electrical engineering from the Indian Institute of Technology Patna, Patna, India, in 2022.

He was a Visiting Scholar and a Research Associate with the Department of Electrical Engineering and Computer Science, Khalifa University, Abu Dhabi, United Arab Emirates, in 2019 and 2021, respectively, where he is currently a Postdoctoral Research Fellow. His research interests include modulation strategies for multiphase motor drives, matrix converters and its control, battery power management, and wireless power transfer.

Dr. Muduli was the recipient of the 2022 IEEE Outstanding Paper Award for the IEEE TRANSACTIONS ON INDUSTRIAL ELECTRONICS.



Abdul R. Beig (Senior Member, IEEE) received the B.Eng. degree in electrical and electronics engineering from the National Institute of Technology Karnataka, Surathkal, India, in 1989, and the M.Tech. and Ph.D. degrees in electrical engineering from the Indian Institute of Science, Bengaluru, India, in 1998 and 2004, respectively.

He is currently an Associate Professor with the Advanced Power and Energy Center, Electrical Engineering and Computer Science department, Khalifa University, Abu Dhabi, United Arab Emirates. His current research focus is on auto tuning of grid-connected converters, electric vehicle drive train, high gain converters, modular multilevel converters, and SiC-based converters.

Dr. Beig has been serving as an Associate Editor for the IEEE TRANSACTIONS ON INDUSTRY APPLICATIONS and IEEE TRANSACTION ON TRANSPORTATION ELECTRIFICATION.



Khaled Al Jaafari (Senior Member, IEEE) received the B.Sc. and M.Sc. degrees in electrical engineering from the Petroleum Institute, Abu Dhabi, United Arab Emirates, in 2006 and 2011, respectively, and the Ph.D. degree in electrical and computer engineering from the Department of Electrical and Computer Engineering, Texas A&M University, College Station, TX, USA, in 2016.

He is currently an Assistant Professor with the Khalifa University of Science and Technology, Abu Dhabi. He has two years (2006–2008) of experience with ZADCO as an Electrical Engineer with the upper Zakum Oil field platform, where he was part of the site facility and maintenance engineering team. His research interests include machines condition monitoring, power system analysis, power system protection, and power quality studies.



Khalifa Al Hosani (Senior Member, IEEE) received the B.Sc. and M.Sc. degrees in electrical engineering from the University of Notre Dame, Notre Dame, IN, USA, in 2005 and 2007, respectively, and the Ph.D. degree in electrical and computer engineering from Ohio State University, Columbus, OH, USA, in 2011.

He is currently an Associate Professor with the Department of Electrical and Computer Engineering, Khalifa University, Abu Dhabi, United Arab Emirates. He is the Cofounder of the

Power Electronics and Advanced Sustainable Energy Center Laboratory, ADNOC Research and Innovation Center, Abu Dhabi. His research interests include a wide range of topics including nonlinear control, sliding mode control, control of power electronics, power systems stability and control, renewable energy systems modeling and control, smart grid, microgrid and distributed generation, and application of control theory to oil and gas applications.



Ameena Saad Al-Sumaiti (Senior Member, IEEE) received the B.Sc. degree in electrical engineering from United Arab Emirates University, Abu Dhabi, United Arab Emirates, in 2008, and the M.Sc. and Ph.D. degrees in electrical and computer engineering from the University of Waterloo, Waterloo, ON, Canada, in 2010 and 2015, respectively.

She was a Visiting Assistant Professor with the Massachusetts Institute of Technology, Cambridge, MA, USA, in 2017. She is currently

an Associate Professor with the Advanced Power and Energy Center and the Department of Electrical Engineering and Computer Science, Khalifa University, Abu Dhabi. Her research interests include power systems, stochastic process, intelligent systems, energy economics, and energy policy.



Ranjan Kumar Behera (Senior Member, IEEE) received the B.Eng. degree in electrical engineering from the Regional Engineering College Rourkela, Rourkela, India, in 1998, and the M.Tech. and Ph.D. degrees in electrical engineering from the Indian Institute of Technology Kanpur, Kanpur, India, in 2003 and 2009, respectively.

Since 2009, he has been a Faculty Member and he is currently an Associate Professor with the Department of Electrical Engineering, Indian

Institute of Technology Patna, Patna, India. His research interests include nonlinear control theory application to power electronic converters, pulsewidth modulation techniques, and multiphase electric drives control.

Dr. Behera was the recipient of the 2022 IEEE Outstanding Paper Award for the IEEE TRANSACTIONS ON INDUSTRIAL ELECTRONICS.